Cross-section Auger imaging: A suitable tool to study aging mechanism of conversion type electrodes

Lénaïc Madec, Jean-Bernard Ledeuil, Gaël Coquil, Grégory Gachot, Laure Monconduit, Hervé Martinez

Cross-Section Auger imaging: a suitable tool to study aging mechanism of conversion type electrodes

Lénaïc Madec[1,4,*], Jean-Bernard Ledeuil[1], Gaël Coquil[2], Grégory Gachot[3,4], Laure Monconduit[2,4] and Hervé Martinez[1,4]

[1] CNRS/ UNIV Pau & Pays Adour/ E2S UPPA, Institut des Sciences Analytiques et de Physicochimie pour l'Environnement et les Matériaux, UMR5254, 64000, Pau, France

[2] ICG-AIME, Bat 15, cc 15-02, Université Montpellier 2, Pl. E. Bataillon, 34095 Montpellier cedex 5, France

[3] Laboratoire de Réactivité et Chimie des Solide (LRCS), CNRS, UMR 7314, Université de Picardie Jules Verne, 33 rue Saint Leu, Amiens, France

[4] Réseau sur le Stockage Electrochimique de l'Energie (RS2E), CNRS FR3459, 33 Rue Saint Leu, 80039 Amiens Cedex, France

* Corresponding Author: lenaic.madec@univ-pau.fr

Abstract: To date, the study of conversion type reactions at both the nanometer and electrode scales over long term cycling still remains very challenging. Here, we show that combining Auger imaging with electrodes cross-section preparation by ion-milling is a suitable tool to study the aging mechanism of conversion type electrodes. Importantly, for NbSnSb-based electrodes, cycled at 25°C and 60°C without and with additives, this innovative approach reveals a micron scale spreading of the NbSnSb particles. It thus proves the electrochemical conversion reaction even after 400 cycles and highlights the role of the inactive Nb element in the long term reversibility, which was unexpected. Interestingly, a shell to core expansion/break up of NbSnSb particles is observed and the large and highly porous structures formed led to the electrodes porosity filling and electrodes thickness increase. The formation of the SEI is located

inside the porous NbSnSb shells. At 25°C without additive, this phenomenon is so important that the ionic and/or electronic conductivities are completely altered, which explains the rapid capacity drop to zero. Overall, cross-section Auger imaging will benefit not only to the study of conversion/alloying based batteries but also to all-solid-state batteries aging mechanism for which buried interfaces have to be reached.

Keywords: Cross-section, Auger, XPS, aging mechanism, conversion material, Li-ion battery.

Introduction

Developing high-energy Li-ion cells became highly required to expand portable electronic devices. To reach this target, improving cathodes and anodes electrochemical performance is of great interest and a huge challenge.[1] Moreover, the high temperature efficiency of Li-ion cells is also increasingly important but remains very challenging as the severe electrolyte degradation leads to resistive electrode/electrolyte interfaces, poor performance and short lifetime[2],[3],[4] despite the use of electrolyte additives.[5],[6],[7]

Conversion/alloying type materials, as negative electrode, have revolutionized Li-ion and beyond due to their high theoretical capacity (2 to 10 times higher than graphite).[8],[9] Their major drawback is, however, their large volume change (typically >200%) during lithiation/delithiation that leads to particles pulverization, loss of electrical contact[10] and continuous electrolyte consumption as the solid electrolyte interphase (SEI) breaks and reforms upon cycling.[9] To tackle these issues, composite conversion materials made of electrochemically active/inactive elements have been successfully developed.[9],[11] From a fundamental aspect, however, the role of the inactive elements in the conversion reaction, usually a transition metal, remains barely understood/investigated for long term cycling. Indeed, most of the studies focus on understanding the Li-storage mechanism of individual nanostructures using e*x situ*[12],[13],[14]

or *in situ*[15],[16] transmission electron spectroscopy (TEM) for which results may not be representative of the three-dimensional electrodes reactivity. To overcome this challenge, *in operando* X-ray tomographic microscopy (SRXTM) allows visualizing simultaneously in three-dimension chemical composition/morphology changes at both individual particles and electrode level.[17],[18],[19] This technique requires, however, access to synchrotron radiation and is limited to short term cycling unless *ex situ* experiments are performed.

Based on these considerations, it is therefore of particular interest to investigate conversion materials that show fundamentally surprising reversibility following the solid state reaction: M_aX_b + (b. n) Li ↔ aM + b Li_nX. In that direction, ternary MSnSb (M= Ti or Nb) electrode materials recently showed unexpected cycling performance at room temperature and more surprisingly also at high temperature.[20],[21] These new conversion materials react with Li as follow: MSnSb + 6.5 Li ↔ M° + Li_3Sb + ½ Li_7Sn_2. For TiSnSb, the unexpected superior coulombic efficiency/lifetime and lower polarization at 60°C compared to 25°C was explained by a specific reactivity of the electrolyte that forms a more stable/passivating SEI.[20] NbSnSb even showed higher capacity retention than the Ti compound.[21] The lifetime was still improved at 60°C compared to 25°C, which was again unexpected since higher temperature usually increased the electrolyte degradation.

Interestingly, surface analysis techniques such as Auger electron spectroscopy (AES),[22],[23] time of flight secondary ion mass spectrometry (ToF-SIMS)[23] and XPS parallel imaging[24] combined to depth profiling or cross-section analysis were proven suitable to study conversion/alloying mechanisms at the nanoscale and/or electrode scales. Note that these approaches are also powerful to characterize the SEI morphology and composition[25],[26],[27],[28] so that AES allowed understanding the aging mechanism of cross-sectioned solid state micro-batteries stacks.[29]

In this work, electrodes cross-sections preparation combined with Auger imaging is used as innovative and easy to implement approach to study the NbSnSb morphological conversion mechanism at both electrode and nanometer scales over long term cycling. Correlation with the electrochemical performance at both 25°C and 60°C using a classical alkyl carbonate-based electrolyte with/without electrolyte additives is then proposed. The electrolyte reactivity is also evaluated using gas chromatography coupled with electron impact mass spectrometry (GC/MS) while the SEI passivation/stability/composition was investigated by XPS.

Experimental

Materials and methods used for the NbSnSb synthesis and electrodes preparation follow previous procedures.[21] Note that the as prepared powder diffractogram and ^{119}Sn Mössbauer spectrum were unequivocally assigned to NbSnSb.[21] The electrode composition was 70:9:9:12 weight ratio of NbSnSb:carbon black:VGCF:CMC. The NbSnSb loading was 2 ±0.2 mg cm^{-2} while the porosity was 77 ±3%. The electrolytes (0.225 ml) were 1M $LiPF_6$ EC:PC:3DMC (in volume) without and with 5% FEC + 1% VC (in volume). Cycling was performed between 0.02-1.5 V at 25°C or 60°C with a first discharge at C/2 rate (i.e. 0.5 mole of Li per mole of NbSnSb per hour) followed by a 48 h storage at 0.02 V then 400 cycles at 4C, stopped in charge. After cells opening, separators and NbSnSb electrodes were used for GC/MS and surface analysis, respectively. Corresponding analysis conditions can be found in details in our previous studies.[20] Before surface analysis, NbSnSb electrodes were washed twice by immersion in DMC (anhydrous, ≥99% purity, Aldrich, 1 ml) in a clean and dry glass vial with a mild manual agitation (10s). Importantly, the same electrodes (cycled 400 times) were used for all performed surface analysis.

Electrodes cross-sections were prepared by ion-milling using a JEOL Cross-Polisher (JEOL Ltd, Tokyo, Japan) in a nitrogen-filled glove box. At 1.10^{-4} Pa, the assemblies, *i.e.* electrode sandwiched between two silicon wafers using a silver conducting epoxy resin, were exposed at normal angle to the Ar^+ ion beam

working at 6 keV (i.e. ion current of ~120 µA) for 8h. Therefore, no resulting sample damage are expected in agreement with the absence of Ar LMM Auger lines at 211 and 195 eV KE. Also, the usual perturbation observed with ion milling cross-section is material redeposition due to the sputtering process, which could lead to curtaining process. More information can be found in the literature.[30],[31],[32] Figure S1 shows typical SEM images of a perfectly planar cross-section assembly.

Scanning electron microscopy (SEM), Auger electron spectroscopy (AES) and scanning Auger microscopy (SAM, *i.e*. elemental 2D distribution) were performed using a JEOL JAMP 9500 F Auger spectrometer (JEOL Ltd, Tokyo, Japan) equipped with a Schottky Field Emission gun and a hemi-spherical analyser coupled with a high dynamic multichannel detector. Note that Auger spatial resolution is about 10-20 nm with a probing depth of about 2-3 nm in the analysis conditions used. The operating pressure was <2 x10-7 Pa. AES survey spectra were recorded between 15 to 2000 eV with 1 eV step size using a focused probe and a CRR mode (constant relative resolution, also called FRR mode) corresponding to a relative energy resolution (dE/E=constant) with dE/E = 0.5% (high sensitivity). SAM (elemental 2D distribution) images were recorded using a CAE mode (constant analyzer energy, also called FAT or CAR mode) corresponding to a fixed energy resolution (dE=constant). The CAE mode allowed defining the useful energy width needed to obtain a significant "peak minus background" (P-B) Auger intensity with respect to the Auger transition and the backgrounds shape. An "auto probe tracking" correction was also applied to control and compensate any potential drift (*i.e.* sample surface charge effects, vibration, electronic and electromagnetic field variations, sample heat dissipation, etc.) during acquisition. Note that electrodes cross-sections thickness was measured by SEM at 0° tilt (not shown) while other analysis were performed at 30° tilt to prevent charging effect.

Results and discussion

Cycling stability versus electrolyte reactivity and SEI passivation/stability

Figure 1a summarizes the 25°C and 60°C long term electrochemical performance of NbSnSb/Li coin cells cycled between 0.02-1.5 V at 4C and filled with 1M $LiPF_6$ EC:PC:3DMC without or with 5% FEC + 1% VC. Overall, only the cycling at 25°C without additive led to a sudden and complete capacity drop after ~75 cycles only while all other cells showed very good and similar capacity retention. This result is therefore unexpected as cycling at high temperature should have led to poorer performance and shorter lifetime due to a higher electrolyte degradation.[2],[4] To evaluate the electrolyte reactivity, GC/MS of the electrolyte extracted from the cells after 400 cycles was performed (Figure 1b). Interestingly, without additive, both electrolytes showed a similar decrease of the EC/PC ratio (due to continuous SEI formation during cycling) so that the significant capacity retention difference cannot be explained at this point. Note also that without additive, an additional carbonate degradation compound was observed at 60°C due to the electrochemical reduction of DMC followed by a multi-step chemical reaction involving MeOLi.[33] With additives, no change of the EC/PC ratio was observed due to the preferential additives consumption. At 25°C, however, additives were not detected anymore while surprisingly, at 60°C, FEC was still observed. This suggests a lower additives consumption at 60°C, which is unexpected. At this point, it could be explained by the formation of less passivating and/or stable SEI at 25°C, so that additives are more consumed, compared to 60°C.

Based on these results, it is possible to sort NbSnSb cells from the lowest expected SEI passivation/stability (*i.e.* highest electrolyte reactivity) to the highest: 25°C without additive (worst capacity retention and decrease of the EC/PC ratio) < 60°C without additive (decrease of the EC/PC ratio and degradation product) < 25°C with additives (no EC/PC ratio change and full additives consumption) ≈ 60°C with additives (no EC/PC ratio change and partial additives consumption). These results are in relatively good agreement with the trend of cumulative irreversible capacity losses of these cells (Figure S2).

Then, to evaluate the SEI passivation/stability and its composition, XPS analysis of the electrodes surface was performed. The XPS peak attribution is based on our previous study[20] so that Figure 1c shows only

the main species observed, in at.%. For clarity, however, the full XPS quantification table (including peaks attribution) as well as the XPS core spectra for elements of interest (C and O) are presented in Table S1 and Figure S3, respectively. Cycling without additive led mostly to the formation of Li_2CO_3 (55 at.% and 40 at.% for 25°C and 60°C) in agreement with the large EC degradation. At this point, cells without additives led to close electrolyte reactivity and SEI composition. Moreover, with additives, thicker SEI were formed as the NbSnSb and carbon additives were almost not observed compared to the cells cycled without additives. This is explained by the formation of an oligomer of VC whose peaks appeared on C 1s and O 1s core spectra (Figure S3).[34],[35] Considering that without additives, thinner SEI were formed despite a higher electrolyte degradation, it thus means that either non-passivating and/or non-stable SEI are formed. It also suggests that the electrolyte degradation species are either solid compounds highly soluble or gas species so that they are not deposited at the electrode surface. Nevertheless, with additives, much more passivating/stable SEI are formed as the electrolyte degradation was greatly hindered. Also, cycling at 60°C with additives led mostly to LiF (47 at.%) with also higher PO_x/PO_xF_y contents, in agreement with a much larger $LiPF_6$ degradation. Such high LiF content compared to the 60°C cycling without additive is explained as follow: the use of additives passivates/stabilizes the SEI so that the solvents degradation is nearly suppressed (*i.e.* only 3 at.% of Li_2Co_3) while the $LiPF_6$ temperature driven degradation still occur. Such large LiF accumulation during cycling may explain the larger polarization observed (Figure S2) and thus the slightly lower capacity retention (Figure 1a). Moreover, at 60°C with additives, the formation of the SEI is driven by the $LiPF_6$ degradation (*i.e.* by the temperature) which may increase its passivation and/or stability and would explain the lower additives consumption compared to 25°C.

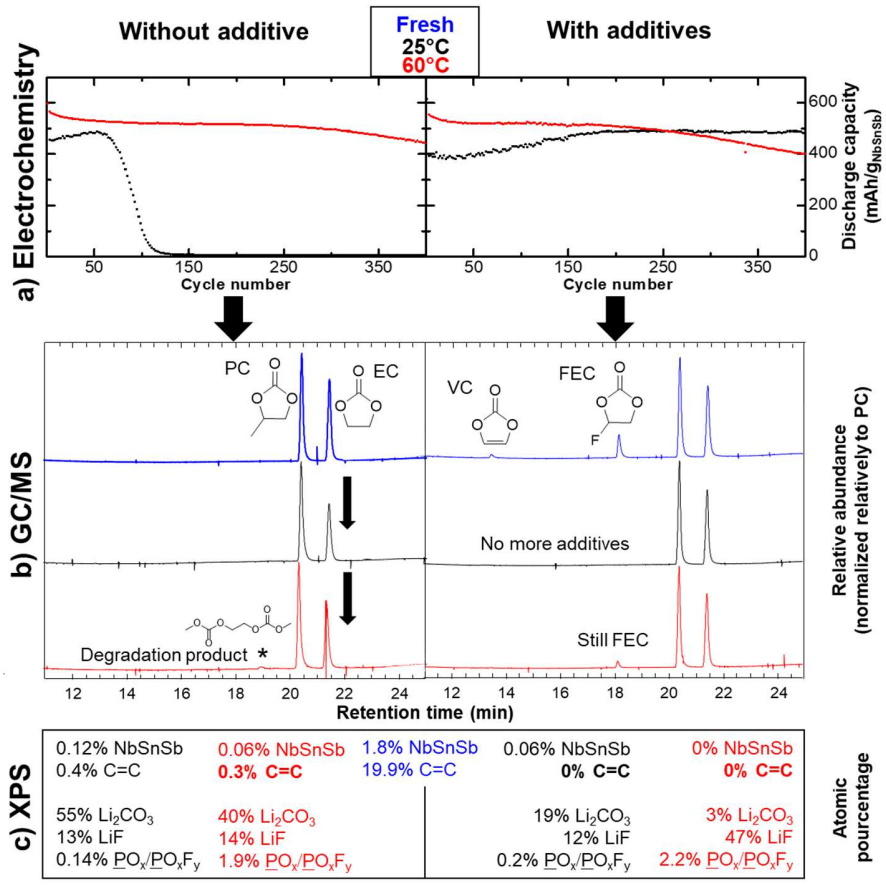

Figure 1. a) Discharge capacity versus cycling number for NbSnSb/Li coin cells cycled at 25°C or 60°C between 0.02-1.5 V at 4C using 1M $LiPF_6$ EC:PC:3DMC without and with 5% FEC + 1% VC as electrolytes. b) Chromatograms (The relative abundances were normalized relatively to PC) of fresh electrolytes and electrolytes extracted from NbSnSb/Li coin cells after 400 cycles at 25°C and 60°C. c) Main species, in at.%, as derived from XPS analysis of a pristine NbSnSb electrode and those extracted from NbSnSb/Li coin cells after 400 cycles at 25°C and 60°C. (Blue: pristine materials; black and red: materials after 400 cycles at 25°C and 60°C, respectively). For clarity, reference [20] fully described the XPS and GC/MS analysis conditions.

Morphological conversion mechanism and SEI distribution

To get more insights on the morphological evolution of NbSnSb particles at both the nanometer and electrode scales as well as the SEI distribution, SEM/Auger analysis of electrodes surface and cross-section

were performed. Interestingly, beyond the apparent covering of the electrodes surface by the SEI, no significant difference was observed between cycled samples (Figure S4) so that it appears more relevant to analyse electrodes cross-sections instead.

The pristine electrode cross-section (10 ±2 µm thick) showed dense and shapeless NbSnSb particles of 0.5-5 µm surrounded by large and porous areas containing carbon additives and CMC (Figure 2a), as confirmed by Auger survey spectra (Figure 2b) and SAM images (Figure 2c and d). Indeed, intense C KLL transitions (150-270 eV KE) and weak O KLL transitions (470-510 eV KE) were observed on carbon areas while NbSnSb particles showed the expected Nb MNN (100-200 eV KE), Sn MNN (400-440 eV KE) and Sb MNN (440-470 eV KE) transitions. The presence of weak O KLL and C KLL peaks on NbSnSb particles is explained by small amount of oxide phases formation during the material synthesis (in agreement with XPS analysis, Table S1 and TEM-EDX analysis, Figure S5) and low contamination of the flat cross-sectioned particles, respectively.

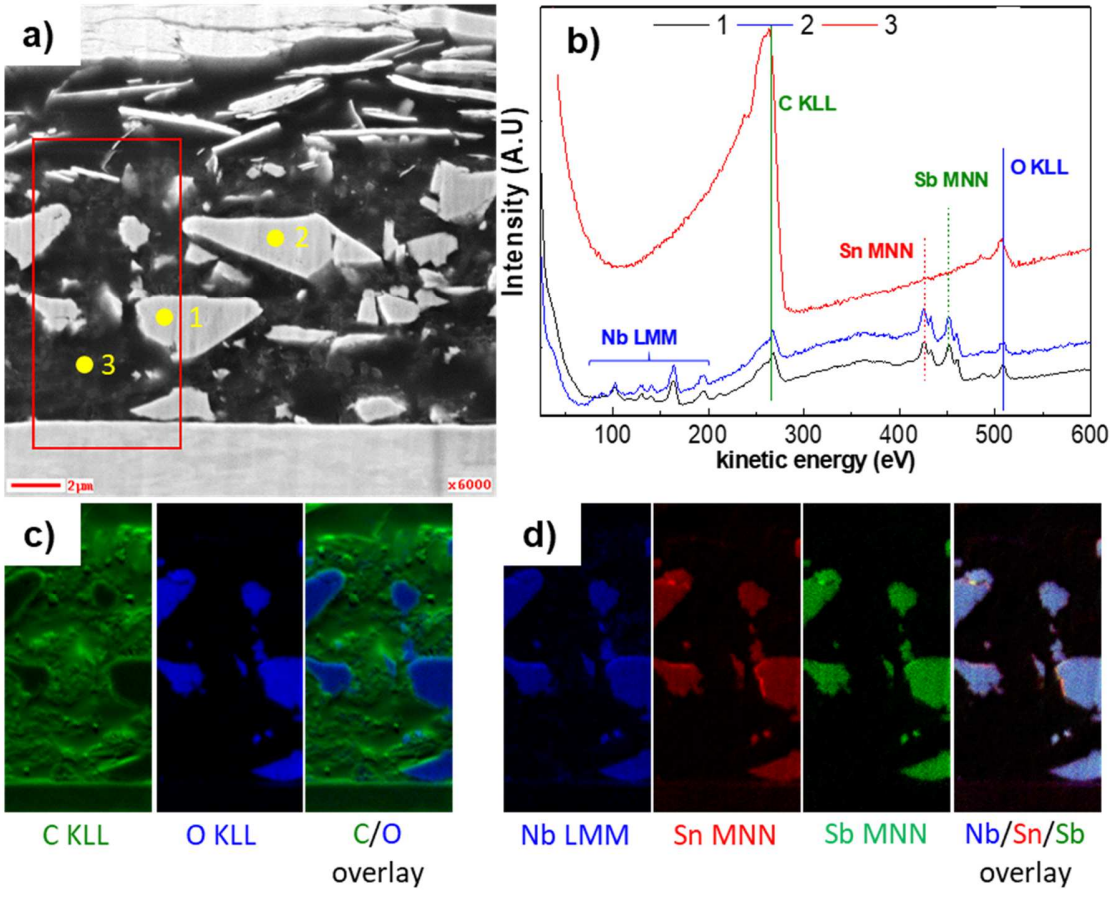

Figure 2. a) SEM image of a pristine NbSnSb electrode cross-section, b) Auger spectra (presented using the EN(E) mode expressed as the output signal of the electron detector using "true" pulse counting versus kinetic energy) taken at different position as indicated and corresponding SAM (elemental 2D distribution) images of c) C KLL, O KLL transitions and their overlay and d) Ti LMM, Sn MNN, Sb MNN transitions and their overlay.

Overall, cycling led to a significant morphology change of NbSnSb particles (Figure 3). Indeed, a non-uniform shell to core expansion/break up of NbSnSb particles was observed as confirmed by SAM images. Indeed, while dense NbSnSb particles were still observed, they were surrounded by the formation of non-uniform porous shell so that dense core-porous shell NbSnSb structures were gradually formed upon cycling. This phenomenon was clearly observed at 25°C without additive due to the fast capacity drop while almost only porous structures (*i.e.* complete shell to core expansion/break up) were observed for other electrodes. As a consequence, the spreading/pulverization of NbSnSb particles led to the electrodes porosity filling as well as to the electrodes thickness increase. Some discrepancies were, however, observed between samples. Interestingly, the expansion ratio (*i.e.* cycled / fresh electrode thickness) increased as follow: 60°C without additive (1.5, *i.e.* from 10 to 15 ±2 µm) < 25°C without additive (3, *i.e.* to 30 ±3 µm) < 60°C with additives (4, *i.e.* to 40 ±3 µm) < 25°C with additives (5, *i.e.* to 50 ±3 µm). Thus, depending on the use of additives and temperature, the electrode porosity partially absorbs the volume change during the continuous NbSnSb spreading. Note that for all samples, a slight discrepancy of the Nb, Sn and Sb elements distribution was observed, indicating non-uniform spreading of the different elements/phases during the continuous conversion reactions. However, considering the micron scale spreading of the NbSnSb particles, it is a direct proof that the conversion reaction still efficiently occurred even after 400 cycles, which was unexpected.

Considering the SEI distribution, oxygen containing areas overlapped well the porous NbSnSb shells while no oxygen was observed on the dense areas, whatever the electrode was (Figure 3). This means that O-containing SEI species (from electrolyte degradation) are mostly formed/deposited at the fresh surface

made by the continuous expansion/break up of NbSnSb particles over long term cycling. Importantly, at 25°C without additive, a lower apparent porosity was observed on the electrodes cross-section, which is in agreement with the higher SEI formation due to the higher electrolyte reactivity (*i.e.* EC reduction). In fact, this sample showed significant beam damage effect due to the SEI degradation during the SAM analysis (Figure S6) while no change was observed for other electrodes cross-sections. This result highlights the large and rapid electrolyte degradation that occurs at 25°C without additive. It leads to a complete obstruction of the electrode porosity so that the ionic and/or electronic conductivities more likely drop to zero in agreement with the cell capacity and the very large increase of polarization (Figure S2). Note that after cycling, fluorine was also detected by AES (not showed) with, however, a very weak intensity so that no mapping could be obtained.

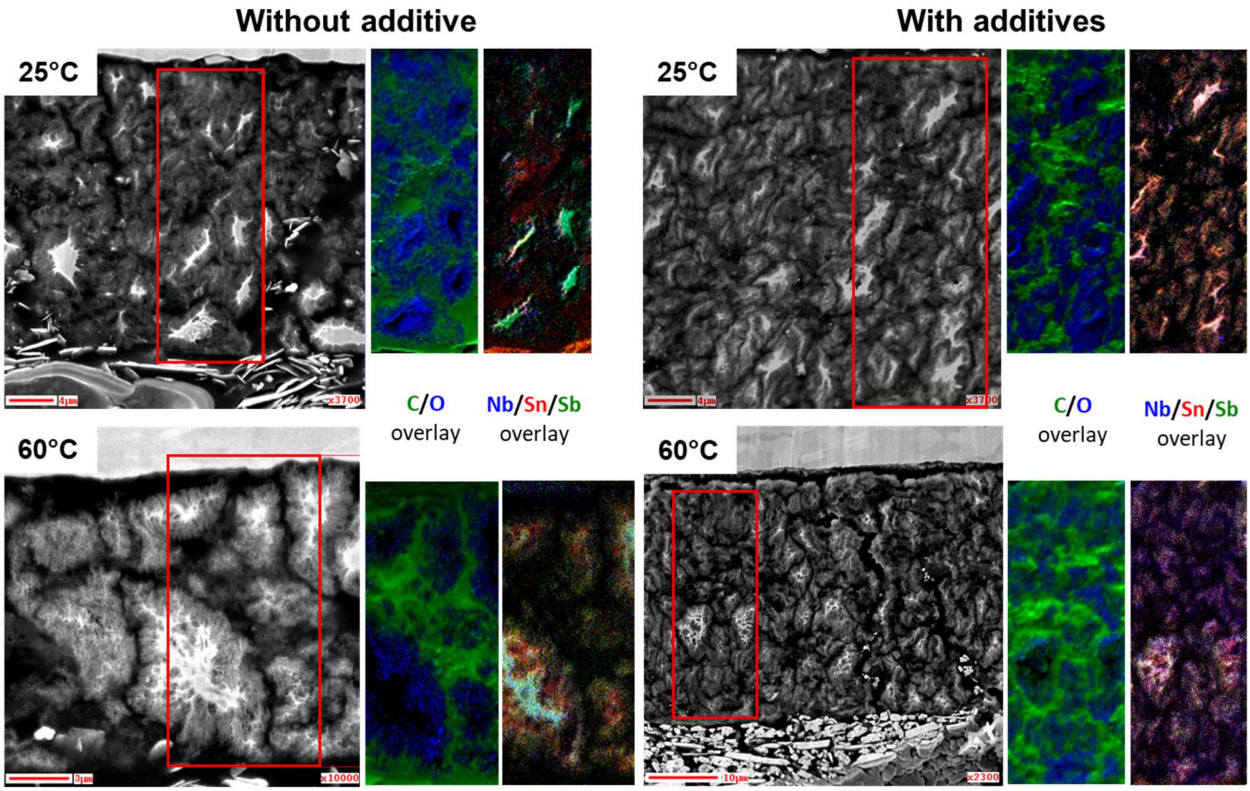

Figure 3. SEM image and corresponding C/O and Nb/Sn/Sb SAM (elemental 2D distribution) overlay of NbSnSb electrodes cross-sections after 400 cycles using 1M $LiPF_6$ EC:PC:3DMC without and with additives at 25°C and 60°C.

Conclusions

In this study, electrochemical performance of NbSnSb electrodes cycled at 25°C and 60°C without and with additives were correlated to the electrolyte reactivity (GC/MS) and SEI passivation/stability (XPS). Cross-section Auger imaging revealed a continuous shell to core expansion/break up of NbSnSb particles during long term cycling (400 cycles), which formed large and highly porous structures. This phenomenon led to the electrodes porosity filling and electrodes thickness increase. Importantly, the micron scale spreading of the NbSnSb particles directly proved that the conversion reaction still occurred even after 400 cycles, which was unexpected. SEI species were mostly formed/deposited inside the porous NbSnSb shells. Interestingly, cycling at 25°C without additive led to an extreme SEI formation (*i.e.* large amount) that obstruct the electrode porosity so that the ionic and/or electronic conductivities were completely altered, in agreement with the rapid cell capacity drop to zero. Overall, this study showed that cross-section Auger imaging is a suitable tool to study the aging mechanism of conversion type electrodes at both the electrode and nanometer scales. In the future, such innovative approach should benefit all-solid-state batteries aging mechanism studies for which buried interfaces have to be reached.

Supporting Information. Typical NbSnSb electrode cross-section SEM images ; Cumulative irreversible capacity losses and average discharge/charge potentials versus cycling number for NbSnSb/Li coin cells ; Carbon and Oxygen 1s core spectra of pristine NbSnSb and 400 times cycled NbSnSb electrodes with full XPS quantification table ; SEM images of pristine and 400 times cycled NbSnSb electrodes surface ; HRTEM-EDS images of a pristine NbSnSb particles ; SEM images of 400 times cycled (at 25°C without additive) NbSnSb electrode cross-section before and after SAM analysis. “This material is available free of charge via the Internet at http://pubs.acs.org.”

Acknowledgment. This research was performed in the framework of "Réseau sur le Stockage Electrochimique de l'Energie" (RS2E) and the ANR program no. ANR-10-LABX-76-01. Authors thank Total S.A. and ADEME for the financial support of G. Coquil's PhD Thesis and the fruitful discussions.

References

[1] D. Andre, S.-J. Kim, P. Lamp, S.F. Lux, F. Maglia, O. Paschos, B. Stiaszny, Future generations of cathode materials: an automotive industry perspective, J. Mater. Chem. A. 3 (2015) 6709–6732. doi:10.1039/C5TA00361J.

[2] N.N. Sinha, T.H. Marks, H.M. Dahn, A.J. Smith, J.C. Burns, D.J. Coyle, J.J. Dahn, J.R. Dahn, The Rate of Active Lithium Loss from a Soft Carbon Negative Electrode as a Function of Temperature, Time and Electrode Potential, J. Electrochem. Soc. 159 (2012) A1672–A1681. doi:10.1149/2.048210jes.

[3] G. Oltean, N. Plylahan, C. Ihrfors, W. Wei, C. Xu, K. Edström, L. Nyholm, P. Johansson, T. Gustafsson, Towards Li-Ion Batteries Operating at 80 ◦C: Ionic Liquid versus Conventional Liquid Electrolytes, Batteries. 2 (2018) 2–7. doi:10.3390/batteries4010002.

[4] P. Ramadass, B. Haran, R. White, B.N. Popov, Capacity fade of Sony 18650 cells cycled at elevated temperatures: Part II. Capacity fade analysis, J. Power Sources. 112 (2002) 614–620. doi:10.1016/S0378-7753(02)00473-1.

[5] S.S. Zhang, A review on electrolyte additives for lithium-ion batteries, J. Power Sources. 162 (2006) 1379–1394. doi:10.1016/j.jpowsour.2006.07.074.

[6] K. Xu, Electrolytes and Interphases in Batteries: Advances during 2003~2014, Chem. Rev. 114 (2014) 11503–11618.

[7] J. Xia, L. Ma, J.R. Dahn, Improving the long-term cycling performance of lithium-ion batteries at elevated temperature with electrolyte additives, J. Power Sources. 287 (2015) 377–385.

doi:10.1016/j.jpowsour.2015.04.070.

[8] J. Cabana, L. Monconduit, D. Larcher, R. Palacin, Beyond Intercalation-Based Li-Ion Batteries: The State of the Art and Challenges of Electrode Materials Reacting Through Conversion Reactions, Adv. Energy Mater. 22 (2010) E170–E192. doi:10.1002/adma.201000717.

[9] V. Aravindan, Y.S. Lee, S. Madhavi, Research Progress on Negative Electrodes for Practical Li-Ion Batteries: Beyond Carbonaceous Anodes, Adv. Energy Mater. 5 (2015) 1402225. doi:10.1002/aenm.201402225.

[10] L.Y. Beaulieu, K.W. Eberman, R.L. Turner, L.J. Krause, J.R. Dahn, Colossal Reversible Volume Changes in Lithium Alloys, Electrochem. Solid-State Lett. 4 (2001) A137–A140. doi:10.1149/1.1388178.

[11] A. Mukhopadhyay, B.W. Sheldon, Deformation and stress in electrode materials for Li-ion batteries, Prog. Mater. Sci. 63 (2014) 58–116. doi:10.1016/j.pmatsci.2014.02.001.

[12] S. Grugeon, S. Laruelle, R. Herrera-Urbina, L. Dupont, P. Poizot, J.-M. Tarascon, Particle Size Effects on the Electrochemical Performance of Copper Oxides toward Lithium, J. Electrochem. Soc. 148 (2001) A285–A292. doi:10.1149/1.1353566.

[13] D. Yonekura, E. Iwama, N. Ota, M. Muramatsu, M. Saito, Y. Orikasa, W. Naoi, K. Naoi, Progress of the conversion reaction of Mn3O4particles as a function of the depth of discharge, Phys. Chem. Chem. Phys. 16 (2014) 6027–6032. doi:10.1039/c4cp00334a.

[14] F. Wang, R. Robert, N.A. Chernova, N. Pereira, F. Omenya, F. Badway, X. Hua, M. Ruotolo, R. Zhang, L. Wu, V. Volkov, D. Su, B. Key, M. Stanley Whittingham, C.P. Grey, G.G. Amatucci, Y. Zhu, J. Graetz, Conversion reaction mechanisms in lithium ion batteries: Study of the binary metal fluoride electrodes, J. Am. Chem. Soc. 133 (2011) 18828–18836. doi:10.1021/ja206268a.

[15] N. Liu, Z. Lu, J. Zhao, M.T. Mcdowell, H.W. Lee, W. Zhao, Y. Cui, A pomegranate-inspired

nanoscale design for large-volume-change lithium battery anodes, Nat. Nanotechnol. 9 (2014) 187–192. doi:10.1038/nnano.2014.6.

[16] Q. Su, J. Xie, J. Zhang, Y. Zhong, G. Du, B. Xu, In Situ Transmission Electron Microscopy Observation of Electrochemical Behavior of CoS 2 in Lithium-Ion Battery, ACS Appl. Mater. Interfaces. 6 (2014) 3016–3022. doi:10.1021/am4056084.

[17] M. Ebner, F. Marone, M. Stampanoni, V. Wood, Visualization and Quantification of Electrochemical and Mechanical Degradation in Li Ion Batteries, Science. 342 (2013) 716–720. doi:10.1126/science.1241882.

[18] C. Villevieille, M. Ebner, J.L. Gómez-Cámer, F. Marone, P. Novák, V. Wood, Influence of conversion material morphology on electrochemistry studied with operando X-ray tomography and diffraction, Adv. Mater. 27 (2015) 1676–1681. doi:10.1002/adma.201403792.

[19] J.B. Cook, T.C. Lin, E. Detsi, J.N. Weker, S.H. Tolbert, Using X-ray microscopy to understand how nanoporous materials can be used to reduce the large volume change in alloy anodes, Nano Energy. 172 (2017) 870–877. doi:10.1021/acs.nanolett.6b04181.

[20] L. Madec, G. Gachot, G. Coquil, H. Martinez, L. Monconduit, Toward efficient Li-ion cells at high temperatures: Example of TiSnSb material, J. Power Sources. 391 (2018) 51–58. doi:10.1016/j.jpowsour.2018.04.068.

[21] G. Coquil, M.T. Sougrati, S. Biscaglia, D. Aymé-Perrot, P.F. Girard, L. Monconduit, On the high cycling stability of NbSnSb in Li-ion batteries at high temperature, Electrochim. Acta. 281 (2018) 619–623. doi:10.1016/j.electacta.2018.05.172.

[22] E. Radvanyi, E. De Vito, W. Porcher, J. Danet, P. Desbois, S. Larbi, J. Colin, Study of lithiation mechanisms in silicon electrodes by Auger Electron Spectroscopy, J. Mater. Chem. A. 1 (2013) 4956–4965. doi:10.1039/c3ta10212b.

[23] A. Bordes, E. De Vito, C. Haon, A. Boulineau, A. Montani, P. Marcus, A. Bordes, E. De Vito, C. Haon, A. Boulineau, A. Montani, Multiscale Investigation of Silicon Anode Li Insertion Mechanisms by ToF-SIMS Imaging Performed on In Situ FIB Cross Section, Chem. Mater. 28 (2016) 1566–1573. doi:10.1021/acs.chemmater.6b00155.

[24] L. Madec, J.-B. Ledeuil, G. Coquil, L. Monconduit, H. Martinez, Cross-Section Auger / XPS imaging of conversion type electrodes: how their morphological evolution controls the performance in Li-ion batteries, ACS Appl. Energy Mater. (2019) doi/10.1021/acsaem.9b01115. doi:10.1021/acsaem.9b01115.

[25] K. Kalaga, I.A. Shkrob, R.T. Haasch, C. Peebles, J. Baren, D.P. Abraham, Auger Electrons as Probes for Composite Micro- and Nanostructured Materials: Application to Solid Electrolyte Interphases in Graphite and Silicon-Graphite Electrodes, J. Phys. Chem. C. 121 (2017) 23333–23346. doi:10.1021/acs.jpcc.7b08279.

[26] C. Tang, R.T. Haasch, J. Ouyang, S.J. Dillon, Insights into Solid-Electrolyte Interphase Induced Li-Ion Degradation from in Situ Auger Electron Spectroscopy, J. Phys. Chem. Lett. 8 (2017) 6226–6230. doi:10.1021/acs.jpclett.7b02847.

[27] C. Tang, K. Leung, R.T. Haasch, S.J. Dillon, LiMn2O4 surface chemistry evolution during cycling revealed by in situ Auger Electron Spectroscopy and X-ray Photoelectron Spectroscopy, ACS Appl. Mater. Interfaces. 9 (2017) 33968–33978. doi:10.1021/acsami.7b10442.

[28] J. Auvergniot, A. Cassel, J. Ledeuil, V. Viallet, V. Seznec, R. Dedryvère, Interface Stability of Argyrodite Li6PS5Cl toward LiCoO2, LiNi1/3Co1/3Mn1/3O2, and LiMn2O4 in Bulk All-Solid-State Batteries, Chem. Mater. 29 (2017) 3883–3890. doi:10.1021/acs.chemmater.6b04990.

[29] A. Uhart, J.B. Ledeuil, B. Pecquenard, F. Le Cras, M. Proust, H. Martinez, Nanoscale Chemical Characterization of Solid-State Microbattery Stacks by Means of Auger Spectroscopy and Ion-

Milling Cross Section Preparation, ACS Appl. Mater. Interfaces. 9 (2017) 33238–33249. doi:10.1021/acsami.7b07270.

[30] T. Schuhrke, M. Mändl, J. Zweck, H. Hoffmann, Investigation of surface amorphization of silicon wafers during ion-milling, Ultramicroscopy. 41 (1992) 429–433. doi:10.1016/0304-3991(92)90223-7.

[31] J.P. McCaffrey, M.W. Phaneuf, L.D. Madsen, Surface damage formation during ion-beam thinning of samples for transmission electron microscopy, Ultramicroscopy. 87 (2001) 97–104. doi:10.1016/S0304-3991(00)00096-6.

[32] M. Mitome, Ultrathin specimen preparation by a low-energy Ar-ion milling method, J. Electron Microsc. (Tokyo). 62 (2013) 321–326. doi:10.1093/jmicro/dfs073.

[33] G. Gachot, S. Grugeon, M. Armand, S. Pilard, P. Guenot, J.M. Tarascon, S. Laruelle, Deciphering the multi-step degradation mechanisms of carbonate-based electrolyte in Li batteries, J. Power Sources. 178 (2008) 409–421. doi:10.1016/j.jpowsour.2007.11.110.

[34] L. El Ouatani, R. Dedryvère, C. Siret, P. Biensan, S. Reynaud, P. Iratçabal, D. Gonbeau, The Effect of Vinylene Carbonate Additive on Surface Film Formation on Both Electrodes in Li-Ion Batteries, J. Electrochem. Soc. 156 (2009) A103. doi:10.1149/1.3029674.

[35] L. Madec, J. Xia, R. Petibon, K.J. Nelson, J.-P. Sun, I.G. Hill, J.R. Dahn, Effect of Sulfate Electrolyte Additives on LiNi1/3Mn1/3Co1/3O2/Graphite Pouch Cell Lifetime: Correlation between XPS Surface Studies and Electrochemical Test Results, J. Phys. Chem. C. 118 (2014) 29608–29622. doi:10.1021/jp509731y.